ADVANCED MATERIALS
www.advmat.de

Check for updates

Controllable Growth of Aligned Monocrystalline $CsPbBr_3$ Microwire Arrays for Piezoelectric-Induced Dynamic Modulation of Single-Mode Lasing

Zheng Yang, Junfeng Lu, Minghua ZhuGe, Yang Cheng, Jufang Hu, Fangtao Li, Shuang Qiao, Yufei Zhang, Guofeng Hu, Qing Yang, Dengfeng Peng, Kaihui Liu,* and Caofeng Pan**

$CsPbBr_3$ shows great potential in laser applications due to its superior optoelectronic characteristics. The growth of $CsPbBr_3$ wire arrays with well-controlled sizes and locations is beneficial for cost-effective and largely scalable integration into on-chip devices. Besides, dynamic modulation of perovskite lasers is vital for practical applications. Here, monocrystalline $CsPbBr_3$ microwire (MW) arrays with tunable widths, lengths, and locations are successfully synthesized. These MWs could serve as high-quality whispering-gallery-mode lasers with high quality factors (>1500), low thresholds (<3 μJ cm^{-2}), and long stability (>2 h). An increase of the width results in an increase of the laser quality and the resonant mode number. The dynamic modulation of lasing modes is achieved by a piezoelectric polarization-induced refractive index change. Single-mode lasing can be obtained by applying strain to $CsPbBr_3$ MWs with widths between 2.3 and 3.5 μm, and the mode positions can be modulated dynamically up to ≈9 nm by changing the applied strain. Piezoelectric-induced dynamic modulation of single-mode lasing is convenient and repeatable. This method opens new horizons in understanding and utilizing the piezoelectric properties of lead halide perovskites in lasing applications and shows potential in other applications, such as on-chip strain sensing.

Since the appearance of semiconductor solid-state lasers in the 1960s,[1] lasers have shown tremendous potential in various applications, such as data communication, medical treatment, environmental science, and military defense. Up to now, enormous research efforts have been conducted to develop high-quality semiconductor lasers.[2] Multiple-mode lasers suffer from false signaling, random fluctuation, and instability which hinder their practical applications.[3,4] Therefore, efforts to achieve single-mode lasers have drawn much attention due to the monochromaticity, high stability, controllable output wavelength, and great potential of these lasers in practical applications, such as in on-chip optical communication.[5] Thus far, most single-mode lasers have been realized in the following four ways: 1) decreasing the cavity size to enlarge the free spectral range (FSR);[6,7] 2) fabricating distributed Bragg reflector (DBR) mirror structures or distributed feedback (DFB)

Z. Yang, Dr. J. F. Lu, Dr. J. F. Hu, F. T. Li, Prof. S. Qiao, Y. F. Zhang, Dr. G. F. Hu, Prof. C. F. Pan
CAS Center for Excellence in Nanoscience
Beijing Key Laboratory of Micro-nano Energy and Sensor
Beijing Institute of Nanoenergy and Nanosystems
Chinese Academy of Sciences
Beijing 100083, P. R. China
E-mail: cfpan@binn.cas.cn

Z. Yang, Dr. J. F. Lu, Dr. G. F. Hu, Prof. C. F. Pan
School of Nanoscience and Technology
University of Chinese Academy of Sciences
Beijing 100049, P. R. China

M. H. ZhuGe, Prof. Q. Yang
State Key Laboratory of Modern Optical Instrumentation
College of Optical Science and Engineering
Zhejiang University
Hangzhou 310027, China
E-mail: qingyang@zju.edu.cn

The ORCID identification number(s) for the author(s) of this article can be found under https://doi.org/10.1002/adma.201900647.

Y. Cheng, Prof. K. H. Liu
State Key Laboratory for Mesoscopic Physics
Collaborative Innovation Centre of Quantum Matter
School of Physics
Peking University
Beijing 100871, China
E-mail: khliu@pku.edu.cn

Prof. D. F. Peng, Prof. C. F. Pan
College of Optoelectronic Engineering
Shenzhen University
Shenzhen 518060, P. R. China

Prof. C. F. Pan
Center on Nanoenergy Research
School of Physical Science and Technology
Guangxi University
Nanning, Guangxi 530004, P. R. China

DOI: 10.1002/adma.201900647

© 2019 WILEY-VCH Verlag GmbH & Co. KGaA, Weinheim

structures on nanostructures;[8] 3) constructing coupled cavity structures through the Vernier effect;[9] and 4) utilizing spatially varied optical pumping.[10] However, decreasing the cavity size will increase the optical loss, which leads to a high threshold and a low quality factor. The fabrication of DBR, DFB, or coupled cavity structures requires complicated nanomanipulations and fabrications. In addition, the dynamic modulation of a single lasing mode using the above methods is limited because of the predesigned cavity configurations, which severely hinders the practical applications.

Altering the refractive index through external stimuli (such as temperature, an electric field, a magnetic field, or a solvent) is an effective approach to dynamic modulation of the lasing modes.[11,12] Previous studies have shown that the piezoresistive effect and piezoelectric polarization effect can regulate the optical bandgap[13] and refractive index[12,14] of hexagonal wurtzites, respectively. These results offer a new strategy for dynamically modulating the lasing mode.

Recently, lead halide perovskites have drawn much attention as an ideal material for laser applications due to their superior optoelectronic characteristics, such as a high absorption coefficient, a long carrier lifetime, a low trap density, a low nonradiative recombination rate, and efficient photoluminescence (PL).[15] Moreover, as perovskite-type (ABX_3) materials, they possess intrinsic piezoelectric and ferroelectric properties that are not yet deeply understood.[16] Strain can modulate the bandgap of $MAPbI_3$[17] and $CsPbBr_3$.[18] In addition, several reports have utilized the piezoelectric effect or the ferroelectricity of lead halide perovskites to fabricate micro–nano devices.[19] Therefore, the piezoelectric polarization of lead halide perovskites can also be utilized in lasing applications. Compared with organic–inorganic hybrid perovskites, all-inorganic perovskites (such as $CsPbBr_3$) exhibit much better stability, which can suppress optical loss and guarantee long-term usage.[20] The growth of highly ordered $CsPbBr_3$ wire arrays with well-controlled sizes and locations is beneficial for cost-effective and largely scalable integration into on-chip devices. Therefore, the controlled growth of aligned monocrystalline $CsPbBr_3$ microwire (MW) arrays with adjustable cross sections as a whispering gallery mode (WGM) resonant cavity could be a promising route to achieve strain-induced single-mode lasing and offer theoretical support for the utilization of the piezoelectric polarization effect in perovskite lasers.

In this work, by using the poly(dimethylsiloxane) (PDMS) template-confined antisolvent crystallization method, the monocrystalline $CsPbBr_3$ MW arrays with tunable widths, lengths, and locations were successfully obtained. These MWs were transferred and fixed onto flexible poly(ethylene naphthalate) (PEN) substrates. They could function as high-quality WGM lasers with a high Q factor and long-term stability. The evolution of the lasing characteristics with increasing width was deeply studied. Then, by applying different strains, the influences of piezoresistive and piezoelectric polarization effects on the gain region and refractive index of $CsPbBr_3$ MWs were clarified. Dynamic modulation of lasing modes was achieved by a piezoelectric polarization-induced refractive index change. By combining size selection and strain application, the single-mode lasing output wavelength coverage can be significantly broadened. This approach not only can be extended to other applications, such as on-chip strain sensing, but also will open new horizons in understanding and utilizing the piezoelectric properties of lead halide perovskites in lasing applications.

Up to now, researchers have used the two-step method, the colloidal method and the asymmetric-wettability method to obtain 1D monocrystalline $CsPbBr_3$.[21] However, a one-step solution method to obtain monocrystalline $CsPbBr_3$ MW arrays has not been demonstrated. Here, we present an improved antisolvent crystallization method to obtain aligned monocrystalline $CsPbBr_3$ MW arrays. First, randomly distributed $CsPbBr_3$ MWs were synthesized to obtain the relevant experimental factors. In brief, as shown in Figure S1 in the Supporting Information, hydrophilic SiO_2/Si substrates coated with stock solution (equal-mole CsBr and $PbBr_2$ in dimethyl sulfoxide (DMSO); saturated with CH_3CN) were placed into a 250 mm crystallizing dish containing 300 mL of CH_3CN. The diffusion of CH_3CN vapor into the stock solution will lead to the crystallization of $CsPbBr_3$ MWs. As the reaction time is prolonged, the MWs gradually grow longer, and the DMSO gradually volatilizes. After 24 h, the substrates were removed, washed with CH_3CN, and blow-dried with an air stream. Figure S2a in the Supporting Information shows an optical photograph of the MWs grown on a SiO_2/Si substrate. A mass of separated MWs with lengths ranging from 150 to 400 μm was successfully obtained. The MWs are the main products, while a few micro-disks also appear. An individual MW with smooth surfaces and sharp edges is shown in a top-view scanning electron microscope (SEM) image (Figure S2b, Supporting Information). Based on the above results, we further introduced the PDMS template into the growth procedure to confine the stock solution. Thus, aligned $CsPbBr_3$ MW arrays were obtained. The lengths and widths of the PDMS templates are controlled by the sizes of the silicon micropillars. A schematic diagram of the PDMS template preparation, an SEM image of the silicon micropillars, and an optical image of the PDMS template are shown in Figure S3 in the Supporting Information. The detailed procedures, including solution preparation, PDMS template preparation, and the PDMS template-confined antisolvent crystallization method, are described in the Supporting Information. **Figure 1**a illustrates the preparation using the PDMS template-confined antisolvent crystallization method. Briefly, the PDMS templates were pressed on top of the stock solution spread on the hydrophilic SiO_2/Si substrates to drive the solution into the templates. The subsequent procedures were similar to the above described randomly distributed MW growth methods. After 24 h, fresh stock solution was injected, and the above process was repeated. Finally, the PDMS substrates were peeled off to leave $CsPbBr_3$ MW arrays on the substrates. This method can be used to easily synthesize $CsPbBr_3$ MWs with controlled widths, lengths, and locations on a large scale. We find that the $CsPbBr_3$ MWs normally appear first at the end positions of PDMS grooves, since nucleation prefers to occur at the high surface-energy corners.

Figure 1b,c and Figure S4a in the Supporting Information show an optical image, an SEM image of aligned $CsPbBr_3$ MW arrays, and an enlarged SEM image of an individual MW grown on a SiO_2/Si substrate, respectively. All the MWs exhibit smooth surfaces, rectangular cross-sections with sharp edges and uniform lengths, indicating the monocrystalline

© 2019 WILEY-VCH Verlag GmbH & Co. KGaA, Weinheim

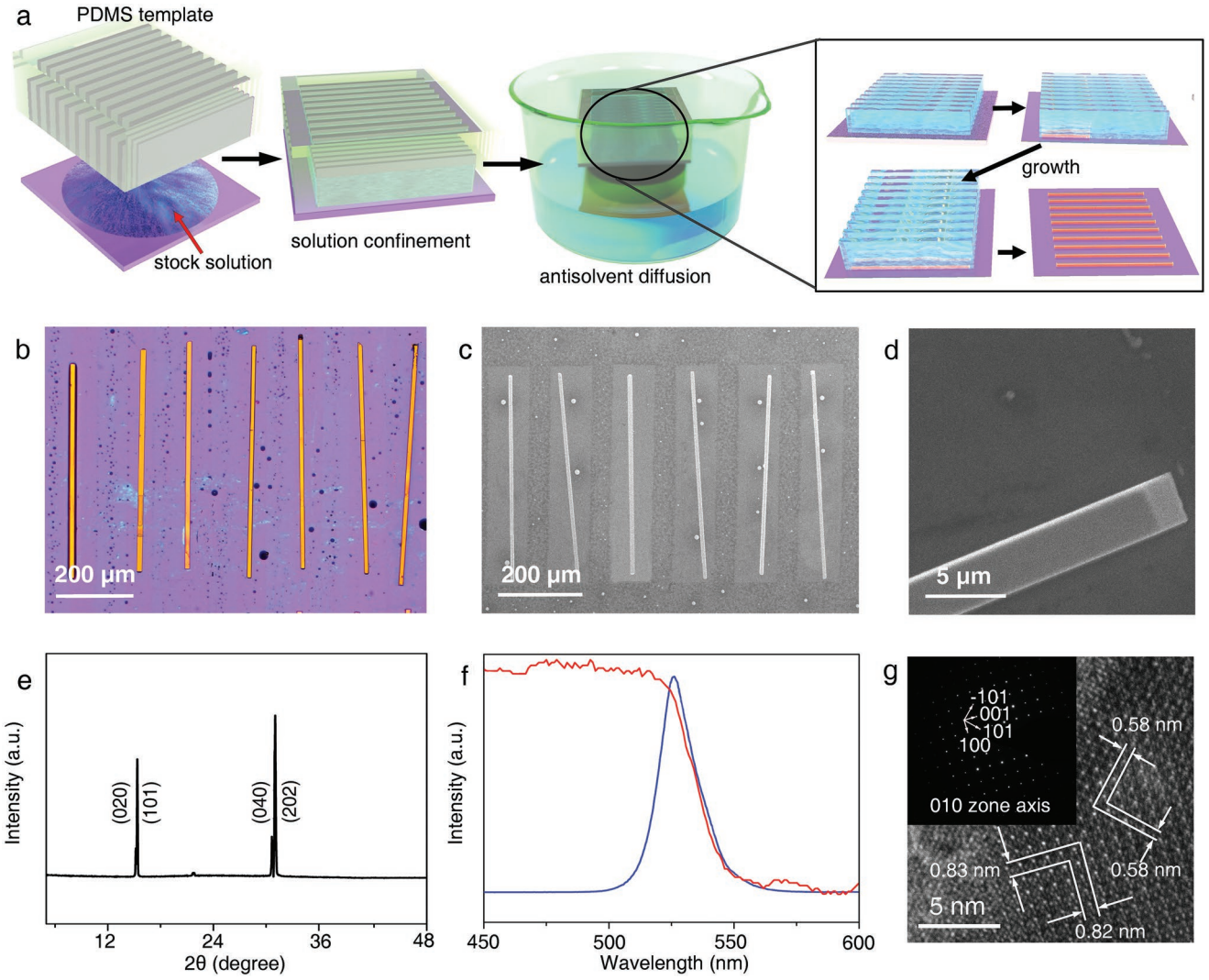

Figure 1. The growth and characterization of $CsPbBr_3$ MW arrays. a) Schematic diagram showing the entire preparation procedure using the PDMS template-confined antisolvent crystallization method. b) Optical image and c) SEM image of aligned $CsPbBr_3$ MW arrays with a length of ≈500 μm on a SiO_2/Si substrate. d) Magnified SEM image of one end of an individual MW (top view), showing a rectangular cross-section and flat end facets perpendicular to the MW long axis. e) XRD, f) PL (blue) and absorption (red) spectra of $CsPbBr_3$ MWs on glass substrates. g) High-resolution TEM image of an individual $CsPbBr_3$ MW. Inset: the corresponding SAED pattern showing the [010] zone axis.

nature. The end facet of the MW is a standard rectangle with a width of 2.6 μm (Figure 1d). Stylus profiler measurement was utilized to measure the height of the MW arrays. A homogenous height of the MW of 2.5 ± 0.1 μm is shown in Figure S4b in the Supporting Information, which is consistent with the SEM result. Several factors that can influence the morphology of the final products exist, i.e., the surface wettability, the initial precursor concentration (the solution concentration before CH_3CN was added), and the PDMS template size. As shown in Figure S5a in the Supporting Information, hydrophobic substrates will result in a small quantity of MWs since the MWs tend to grow in the PDMS templates rather than on the substrates. The widths of the MWs are mainly determined by the initial precursor concentration rather than by the PDMS template width (Figure S5b, Supporting Information). When the initial precursor concentration is 0.24 M, the average width is ≈2 μm. Upon increasing the initial precursor concentration to 0.32 M, the average widths of the MWs exceed 4 μm. With a further increase in the initial precursor concentration to 0.4 M, the average width is ≈7 μm. However, the widths of the PDMS template influence the morphologies of the final products. Figure S5c,d in the Supporting Information depicts optical images of as-grown $CsPbBr_3$ MW arrays obtained using the PDMS templates with widths of 30 and 100 μm, respectively. When the width is small, limited by the stock solution volume, the MWs cannot grow sufficiently long, resulting in various lengths. In contrast, the 100 μm width will lead to most of the as-grown $CsPbBr_3$ products being microplates. Raising the reaction temperature would obviously accelerate the growth speed. The lengths of the MWs are determined by the template length. A shorter template length leads to shorter MW arrays (Figure S5e, Supporting Information). The maximum lengths

© 2019 WILEY-VCH Verlag GmbH & Co. KGaA, Weinheim

are ≈500 µm. In addition, if the stock solution is not presaturated with CH_3CN, only some unknown impurities are generated after 24 h (Figure S5f, Supporting Information). Besides, limited by solution volume, after two cycles' growth (48 h), about 65% of locations have MWs on them. Prolonging the growing time will increase the MWs' coverage.

Figure 1e shows the X-ray diffraction (XRD) curve proving that the as-prepared $CsPbBr_3$ MW arrays belong to the orthorhombic crystal structure, with four peaks assigned to the (020), (101), (040), and (202) orthogonal crystallographic planes. The absorption and PL spectra of the MWs in Figure 1f show a peak position of 530 nm in the PL spectrum and an absorption onset of 566 nm in the absorption spectrum, in accordance with previous reports.[22] Transmission electron microscopy (TEM) analysis was conducted on an individual MW to show its crystal structure and growth direction. The TEM sample was obtained via the focused ion beam cutting method because the thickness of the MWs is far greater than 200 nm (Figure S6a,b, Supporting Information). The high-resolution TEM and corresponding selected-area electron diffraction (SAED) results in Figure 1g prove that the MW belongs to the orthorhombic crystal structure with the [010] zone axis, which agrees well with previous reports. Since the normal direction of the TEM sample is parallel to the MW axial direction, the growth is along the [010] orientation (Figure S6c, Supporting Information). The energy-dispersive X-ray spectroscopy analysis results in Figure S7 in the Supporting Information show that the Cs, Pb, and Br elements are uniformly distributed within the MW and that the Cs/Pb/Br ratio is 1.05:1:3.2, which is in good agreement with the $CsPbBr_3$ stoichiometry.

$CsPbBr_3$ MWs with different widths were then transferred onto circular PEN substrates (R = 1 cm, thickness = 200 µm) using heat-release tape and fixed by polymethyl methacrylate for further lasing tests. A schematic diagram of the transfer procedure is shown in Figure S8 in the Supporting Information, and the detailed methods can be found in the Supporting Information. **Figure 2**a and Figure S9 in the Supporting Information show a complete set of a confocal micro-system coupled with a femtosecond 355 nm laser, a spectrograph equipped with a charge coupled device detector, an image capture system, and a homemade positioning system, which can be used to investigate the optical properties of the $CsPbBr_3$ MWs with and without applied strain.

All optically pumped lasing experiments were performed in ambient atmosphere (30 RH%) at room temperature. A beam of a 355 nm femtosecond laser served as the uniform pump source to excite an individual $CsPbBr_3$ MW (Figure 2a,b). Figure S10 in the Supporting Information shows the optical bright field (a) and dark field (b and c) images of a representative single $CsPbBr_3$ MW (length is ≈200 µm, width is 2.3 µm). When the MW was pumped with a low power density, uniform green PL was observed. When the excitation density exceeded the lasing power threshold (P_{Th}), two bright and strong lasing emissions with spatial interference patterns were observed on the two sides of the MW. Figure 2c shows the typical excitation-power-dependent PL spectra of the abovementioned MW. When the pump density was below the threshold, only broad spontaneous emission peaks were observed. When the pump density exceeded the threshold, a single sharp peak started to appear and grew drastically with a further increase in the pump density. With a continuous increase in the pump density, no other lasing peak appeared, proving the single-mode lasing behavior. A slight blueshift (less than 1 nm) was observed with increasing pump density, which may be caused by the band-filling effect.[7]

Figure 2d plots the PL intensity and full-width at half-maximum (FWHM) as a function of the pumping energy density. An inflection point can be observed during the pumping density increase procedure, confirming the evolution from spontaneous emission to stimulated emission at ≈2.2 µJ cm^{-2}. At this point, the FWHM will also dramatically decrease. Figure 2e depicts the corresponding lasing peak showing the quality factor (Q factor). The peak is well-fitted by a Lorentzian function with an FWHM of 0.35 nm. The Q factor was calculated to be ≈1555 using the equation $Q = \lambda/\delta\lambda$, where λ is the peak center wavelength and $\delta\lambda$ is the peak width. Finite-difference time-domain (FDTD) simulations were carried out to investigate the resonant cavity in the transverse plane of the $CsPbBr_3$ MW. The WGM resonance in the transverse electric (TE) mode is well-confined in the cavity and reflected between the four side faces (Figure S11, Supporting Information), while the transverse magnetic (TM) modes cannot contribute to the laser emission.

Further investigations of the lasing dynamics in $CsPbBr_3$ MWs were conducted with time-resolved photoluminescence (TRPL) using a 410 nm femtosecond laser. Figure 2f shows the typical PL decay curves of the $CsPbBr_3$ MW below and above the pumping threshold. When the $CsPbBr_3$ MW is pumped with a low pump density ($0.8P_{Th}$), the decay profile fitted by an exponential function yields a lifetime of τ = 1.7 ns. A much shorter lifetime of τ = 124 ps is obtained when the pump density is above the threshold ($1.2P_{Th}$), implying the appearance of the stimulated emission process.[4] Furthermore, to test the stability of the lasing output, the $CsPbBr_3$ MW was constantly pumped by the 355 femtosecond laser with an excitation density of $1.2P_{Th}$. The integrated emission intensity of the MW versus the excitation time is shown in Figure 2g, in which stable lasing output can be observed for over 110 min. These results illustrate that the $CsPbBr_3$ MWs have significantly long operating lifetimes under ambient conditions. In addition, the MWs exhibit outstanding long-term stability without any additional protection (stored in an inert gas or encapsulated with a polymer). The obtained MWs were stored in ambient environment and underwent lasing tests every 3 days. As shown in Figure S12 in the Supporting Information, after 1 month, the lasing peak intensity decrease was less than 6%, and the corresponding pump density threshold almost did not change. Single-mode lasing with MWs with different widths was also performed. As shown in Figure S13a in the Supporting Information, the single-mode lasing emission can be tuned from 539 to 547 nm by increasing the width of the MW. The curve showing the single-mode lasing emission wavelength versus the MW width is plotted in Figure S13b in the Supporting Information. With increasing width, the lasing emission peaks show an obvious redshift. The resonant modes of a square WGM microcavity can be calculated according to Equation (S1) (Supporting Information). Since the size of MW varies very little and only one lasing mode survives in the gain region,

© 2019 WILEY-VCH Verlag GmbH & Co. KGaA, Weinheim

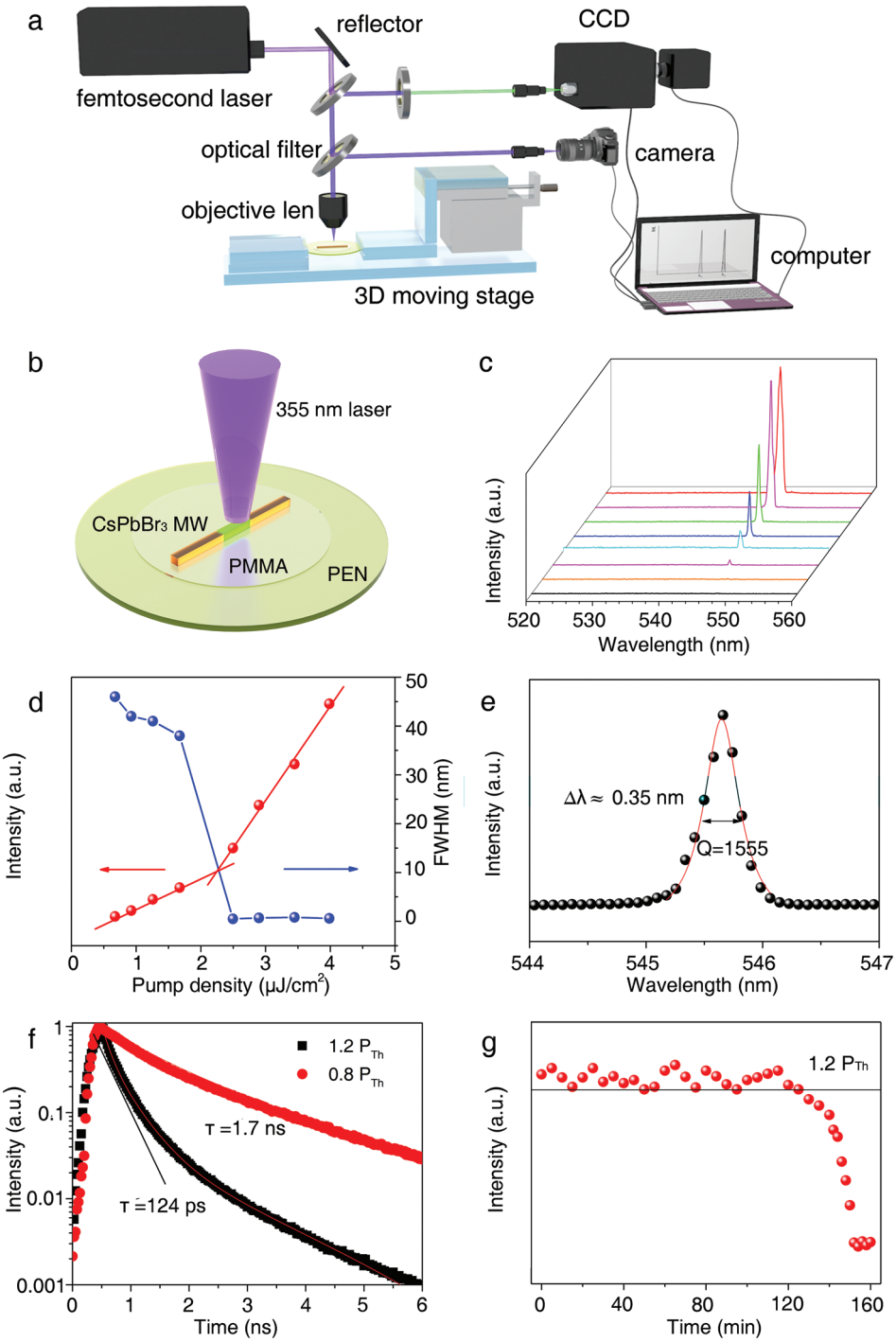

Figure 2. Lasing output of an individual $CsPbBr_3$ MW. a) Schematic diagram of the entire optical path and test system. b) Schematic illustration of a $CsPbBr_3$ MW on a PEN substrate pumped by a 355 nm laser. c) PL spectra of the MW in (a), measured with increasing pump density. d) Integrated PL emission intensity (black) and FWHM (blue) as a function of the pump density, showing the lasing threshold of 2.2 μJ cm^{-2}. e) Lorentzian fitting of a lasing peak, showing a quality factor of 1555. f) PL decay curves obtained at two different excitation densities ($0.8P_{Th}$ and $1.2P_{Th}$), showing the evolution from spontaneous emission to stimulated emission. g) Integrated emission intensity of a $CsPbBr_3$ MW under 355 nm femtosecond laser excitation at a constant pump density of $1.2P_{Th}$ in ambient atmosphere.

so the resonant mode is unchanged and thus the lasing wavelength has a linear correlation with the width of MW. When the width is less than 1.9 μm, lasing can hardly be obtained due to the high optical loss. However, when the width is greater than 2.4 μm, dual-mode lasing will occur, which will be discussed in the next section.

To further understand the lasing characteristics of the $CsPbBr_3$ MWs, the lasing spectra with multiple modes were

© 2019 WILEY-VCH Verlag GmbH & Co. KGaA, Weinheim

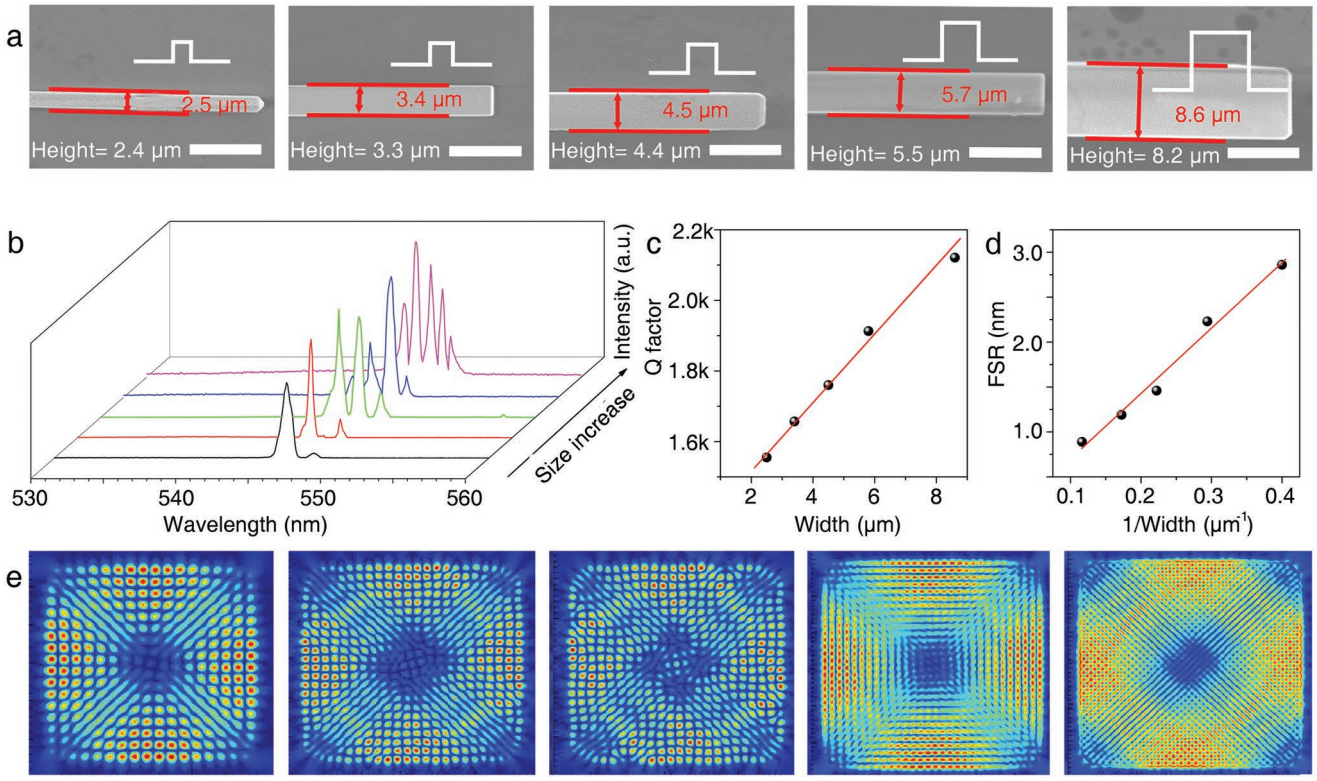

Figure 3. Width-dependent lasing characteristics and FDTD simulations. a) SEM images of $CsPbBr_3$ MWs with different widths. The scale bar is 5 μm. b) Lasing spectra of $CsPbBr_3$ MWs with five different widths. c) Q factor and d) FSR as a function of the $CsPbBr_3$ MW width. e) FDTD stimulations showing the electric-field distribution of the fundamental mode in the x–y plane for different $CsPbBr_3$ MWs.

measured and analyzed. **Figure 3**a shows SEM images of five typical $CsPbBr_3$ MWs with widths ranging from 2.5 to 8.6 μm. All of them have smooth surfaces and sharp edges, ensuring total internal reflection of light waves between the four surfaces. Figure 3b demonstrates the evolution of the lasing spectra with increasing MW width. With the increase of the width (from 2.5 to 8.6 μm), the number of modes gradually increases. All of them can contribute to TE mode lasing and with continuous increasing pumping density, no TM lasing modes were found. The PL spectra of five MWs were also recorded which are shown in Figure S14a in the Supporting Information. All of five curves almost overlap with each other, proving that they have same bandgaps. From the results in Figure 3c,d, one can find that the Q factor and FSR have a direct relationship with the $CsPbBr_3$ MW width. The Q factor has a linear relation with the MW width, and a larger resonant cavity leads to a higher Q factor. This phenomenon occurs because of the stronger capability to confine the optical field and the lower optical loss in a larger resonant cavity. A slight reduction in lasing thresholds also proves it (Figure S14b, Supporting Information). For a square WGM cavity with a cavity length of L, the value of the FSR can be calculated according to the equation

$$\Delta\lambda = \lambda^2 / L\left(n - \lambda dn/d\lambda\right) \tag{1}$$

where $L = 2\sqrt{2}D$ (D is the width of the MWs since the transverse planes of the MWs are approximately square), and $n - \lambda dn/d\lambda$ is the effective refractive index.[23] The FDTD stimulations in Figure 3e show the electric fields of the fundamental mode in MWs with different widths. With increasing MW width, the confinement effect of the cavity on the electric field is enhanced; thus, the number of layers distributed inward along the edge of the cavity increases, indicating an increase in the lasing mode number, which accords with the experimental results. A reduction of the microcavity size results in decreasing mode number but also higher optical loss. Therefore, in addition to the selection of the MW width, a strain is introduced to realize single-mode lasing and wavelength modulation in $CsPbBr_3$.

A $CsPbBr_3$ MW with a width of 3.3 μm was used as a model microcavity to analyze the effect of the strain. Figure S15 in the Supporting Information shows a schematic diagram for estimating the applied tensile and compressive strain (ε %). As shown in Figure S16 in the Supporting Information, when no strain is applied, two distinct lasing modes of TE43 and TE42 emerge when the pumping power exceeds the lasing threshold. From **Figure 4**a, with the increase of compressive strain, a small blueshift in PL emissions occurs (from 527.1 to 526.2 nm with the compressive strain increasing from 0% to –0.96%). This blueshift is attributed to lattice compression (the bandgap increases with increasing compressive strain), and this phenomenon is in accord with the reported result.[18] In contrast, the PL emissions undergo a redshift with increasing tensile strain (from 527.1 to 528.3 nm with the compressive strain increasing from 0% to 1.06%). Similar to the PL emission peak, the lasing peaks also demonstrate a redshift phenomenon with tensile strain and a blueshift phenomenon with compressive

© 2019 WILEY-VCH Verlag GmbH & Co. KGaA, Weinheim

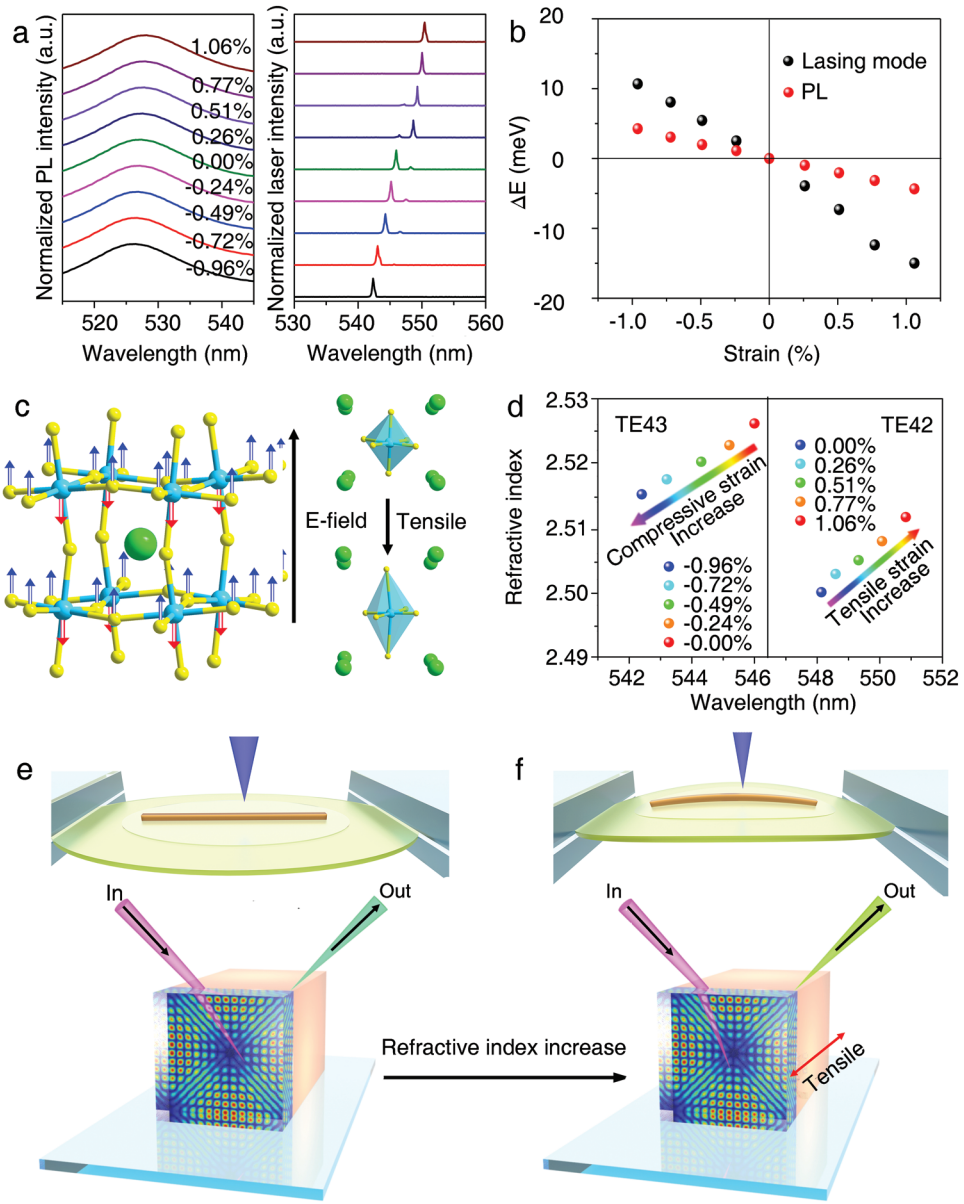

Figure 4. a) Spectra of stimulated and spontaneous emission for the $CsPbBr_3$ MW under different degrees of compressive and tensile strain. b) The blue-/redshift variation of the PL emission and lasing mode photon energy as a function of the compressive and tensile strain. c) Schematic diagram showing the polarization as a consequence of the polar displacements of Pb (red arrows) and Br (blue arrows) and the $PbBr_6$ octahedron distortion under tensile stress (right). d) The relationship of the resonant wavelengths for the TE_{43} and TE_{42} modes with the refractive index under different compressive and tensile strains. e,f) Schematic diagrams showing the mechanism from the normal state (e) to tensile state (f).

strain. As shown in Figure S17a in the Supporting Information, when the tensile strain increases, the lasing intensity of TE43 decreases, while the lasing intensity of TE42 increases. When the tensile strain reaches 0.77%, single-mode lasing (TE42) is obtained, accompanied by the disappearance of the TE43 mode. The TE42 wavelength can be tuned from 548.1 to 550.8 nm with the tensile strain varying from 0% to 1.06%. In contrast, an applied compressive strain will lead to a blueshift of the lasing peak. When the compressive strain increases from 0% to –0.49%, the TE42 mode gradually disappears and single-mode lasing is obtained. The wavelength of lasing mode TE43 can be regulated from 548.1 to 550.8 nm. However, as shown in Figure 4b, the wavelength variation rate of the PL emission peak with increasing applied strain is lower than that of the lasing peak. Namely, the lasing region moves faster than the PL with increasing strain. At room temperature, the 527 nm PL peak can be attributed to the emissions of free excitons with high energy,[24] and the emission wavelength is dominated by bandgap rather than defects related energy levels. Therefore, the underlying mechanisms leading to the shifts of the lasing mode and PL emission are different in nature. As an ABX_3-type semiconductor, $CsPbBr_3$ consists of a framework of corner-sharing $PbBr_6$ octahedra and Cs cations in the dodecahedral A sites (Figure 4c, left). At room temperature, the $CsPbBr_3$ crystal

© 2019 WILEY-VCH Verlag GmbH & Co. KGaA, Weinheim

structure is orthorhombic (Figure S18, Supporting Information), which is a low-symmetry structure. Strain along the ⟨010⟩ direction of the MWs will lead to distortion of the lattice (Figure 4c, right), resulting in the piezoelectric potential. Thus, piezoelectric polarization is proposed to exist in $CsPbBr_3$ with applied strain. In addition, the size change of the optical microcavity also has an important effect on the laser mode shift. Considering the Poisson ratio of $CsPbBr_3$ (≈0.33), the decrease of D can be estimated as 2.83, 5.55, 8.38, and 11.5 nm under tensile strains of 0.26%, 0.51%, 0.77%, and 1.06%, respectively. If only considering the change of the cavity, according to Equation (S2), tensile strain in the ⟨010⟩ direction will lead to a slight blueshift of lasing modes (0.5, 0.9, 1.5, 2.1 nm). In contrast, compressive strain will lead to an increase of D, resulting in a slight redshift of lasing modes. However, both of these analyses are opposite to our results. Since during our measurements, the test conditions such as pumping density, temperature, and humidity are unchanged and no other factors such as magnetic or electric field are introduced. In consideration of opposite effects caused by Poisson effect, piezoelectric polarization effect is much more obvious than bandgap change. Therefore, the lasing movement is attributed to the changing refractive index induced by the piezoelectric polarization effect (Figure 4c,d). According to Rayleigh criterion, the wavelength shift can be identified when it is approximately larger than FWHM. Figure S19a in the Supporting Information shows that TE42 wavelength shift has a linear relation with tensile strain. Thus, the minimum strain should be larger than 0.19%, and minimum modulation resolution of the lasing mode is ≈0.3 nm. Besides, when between −0.96% and 1.06%, the strain has no influence on lasing thresholds (Figure S19b, Supporting Information).

Therefore, the lasing movement is attributed to the changing refractive index induced by the piezoelectric polarization effect (Figure 4c,d).

However, as shown in Figure S20a in the Supporting Information, by further increasing the compressive strain from −1.38% to −2.55%, along with the blueshift of the PL emission, another peak derived from surface defects gradually appears, and its intensity increases. Meanwhile, the laser intensity gradually decreases until no lasing emission is found (Figure S20b, Supporting Information). This phenomenon may be attributed to the increasing compressive strain leading to more surface defects, thus resulting in higher optical loss and lasing thresholds. On the other hand, when the tensile strain is increased to ≈1.5%, the MWs are broken off. Before this time, the lasing peak continuously undergoes a redshift, and no obvious degradation in the laser intensity is found. The angular-dependent lasing spectra (Figure S21a–c, Supporting Information) confirm that the component of stress parallel to the MW direction determines the lasing mode shift. The influence of the laser excitation position on the lasing mode shift was also considered. As shown in Figure S21d–f in the Supporting Information, both ends of the MW were excited, and lasing spectra for different tensile strains were recorded. With the increase of the tensile strain, all three positions show the same trend. The small difference in the lasing spectra among the three positions may be attributed to the difference in stress distribution since the entire bending system is not under a perfect coaxial stretch. These results prove that the strain-induced lasing mode shift is position independent. In addition, the strain-induced lasing mode shift is length independent in our tests (dozens of MWs with lengths ranging from 100 to 500 μm). However, when MW lengths become shorter (<50 μm), the mode shift under same strain is smaller. This is due to that effective strains on MWs are much smaller than the calculated values. The strain-induced lasing wavelength modulation can also be applied to MWs with other mode numbers. As shown in Figure S22 in the Supporting Information, a similar redshift phenomenon can be obtained in MWs with widths of ≈2.2 μm (single mode) and ≈6.l μm (quadruple mode), proving that strain can dynamically modulate the lasing emission in different cases. Compared with other tuning methods such as electric field, magnetic field, and atmosphere components, our piezoelectric modulation method is convenient and cost-effective without additional devices. This method can be used in other applications such as strain sensing.

Through mode selection and dynamic regulation, a range of up to 8.5 nm for the single-mode lasing can be obtained, as shown in Figure S23a in the Supporting Information. The side-mode suppression ratio (SMSR) can be calculated as 12.6 and 14.7 dB in the cases of tension and compression, respectively, according to $SMSR = 10\log(M_1/M_2)$, where M_1 and M_2 are the intensities of the dominant mode and side mode, respectively. To further verify the piezoelectric polarization effect tuning of the refractive index of $CsPbBr_3$, the refractive indices of the TE43 and TE42 modes under different degrees of applied strain were calculated by fixing the value of the width (D), mode number (N), and lasing peak wavelength (λ), as shown in Figure S23b in the Supporting Information. In addition, Figure 4d and Figure S17b,c in the Supporting Information plot the resonant wavelengths of TE43 and TE42 as a function of the refractive index under different compressive and tensile strains, respectively. The linear fitting results reveal the greater impact of the piezoelectric polarization effect on the refractive index than the bandgap change or size change, distinctly proving the dominant reason for the change in the refractive index. The schematic diagrams in Figure 4e,f show the corresponding mechanism. A sketch summarizing the gain spectra and lasing mode positions in the normal and tensile states is drawn in Figure S24a in the Supporting Information. In the normal case, the solid Gaussian curve is the gain spectrum of $CsPbBr_3$, with the WGM modes marked as solid vertical lines and the lasing threshold denoted as a dashed black horizontal line. Only the modes that exceed the threshold value will be amplified and selected. As tensile strain is applied, a redshift of the gain spectrum and the resonant wavelength will occur. Due to the faster redshift speed of the lasing mode, only one mode is located in the gain region, which will be amplified and selected. Finally, single-mode lasing can be realized and tuned dynamically within a certain wavelength range (Figure S24b, Supporting Information).

The repeatability and reproducibility of the strain-induced single-mode lasing is indispensable for practical applications. Therefore, as shown in Figure S25a in the Supporting Information, 20 cycles (tensile–compressive–release) of lasing tests

© 2019 WILEY-VCH Verlag GmbH & Co. KGaA, Weinheim

were conducted on the same MW. The lasing peak positions for tensile strain or compressive strain remained almost the same, and after each cycle, the laser peak position could always return to the original wavelength, proving the repeatability and stability of the strain-induced single-mode lasing. In addition, we conducted strain-induced lasing shift tests on 28 $CsPbBr_3$ MWs with width ranging between 2.3 and 3.5 μm which exhibit dual-mode lasing behavior, and the resultant data distribution is shown in Figure S25b in the Supporting Information. By applying specific tensile strains, 26 MWs showed single-mode lasing behaviors. Namely, one of the two lasing modes could be effectively suppressed by the strain, leaving only one lasing mode. These results prove the reproducibility of the strain-induced single-mode lasing.

In conclusion, the controllable growth of aligned monocrystalline $CsPbBr_3$ MW arrays was realized by the PDMS template-confined antisolvent crystallization method. These arrays can serve as high-quality WGM lasers with almost identical optical modes, high *Q* factors, and excellent stability. Experimental results demonstrated that a cavity size increase will result in an increase of the laser quality and the resonant mode number. The piezoelectric polarization effect-induced change of the refractive index enables effective tuning of the lasing mode position up to 8.5 nm for the $CsPbBr_3$ MWs with an externally applied strain ranging between −0.96% and 1.06%. The tensile strain leads to the redshift of the lasing mode while the compressive strain leads to blueshift. Dynamic modulation of single-mode lasing was achieved on $CsPbBr_3$ MWs with appropriate width. This piezoelectric polarization-induced single-mode lasing demonstrates good repeatability and reproducibility. This work offers not only an approach to pattern high-quality $CsPbBr_3$ arrays but also a new way to utilize the piezoelectric properties of lead halide perovskites to dynamically tune the lasing modes, which are important for future integration into electronic and photonic circuit applications.

Supporting Information

Supporting Information is available from the Wiley Online Library or from the author.

Acknowledgements

Z.Y. and J.F.L. contributed equally to this work. The authors thank the support of National Natural Science Foundation of China (nos. 61675027, 51622205, 51432005, 61505010, and 51502018), National Key R & D Project from Minister of Science and Technology, China (2016YFA0202703), Beijing City Committee of Science and Technology (Z171100002017019 and Z181100004418004), Beijing Natural Science Foundation (4181004, 4182080, 4184110, 2184131, and Z180011), and the China Postdoctoral Science Foundation Funded Project (nos. 2018M630122 and 2017M620709).

Conflict of Interest

The authors declare no conflict of interest.

Keywords

arrays, $CsPbBr_3$, mode shift, piezoelectric, single-mode lasers

Received: January 27, 2019
Revised: February 28, 2019
Published online:

[1] M. I. Nathan, W. P. Dumke, G. Burns, F. H. Dill, G. Lasher, *Appl. Phys. Lett.* **1962**, *1*, 62.
[2] a) X. F. Duan, Y. Huang, R. Agarwal, C. M. Lieber, *Nature* **2003**, *421*, 241; b) I. D. W. Samuel, G. A. Turnbull, *Chem. Rev.* **2007**, *107*, 1272; c) H. Zhu, Y. Fu, F. Meng, X. Wu, Z. Gong, Q. Ding, M. V. Gustafsson, M. T. Trinh, S. Jin, X. Y. Zhu, *Nat. Mater.* **2015**, *14*, 636.
[3] a) R. Chen, B. Ling, X. W. Sun, H. D. Sun, *Adv. Mater.* **2011**, *23*, 2199; b) M. H. Huang, S. Mao, H. Feick, H. Q. Yan, Y. Y. Wu, H. Kind, E. Weber, R. Russo, P. D. Yang, *Science* **2001**, *292*, 1897.
[4] B. Tang, H. Dong, L. Sun, W. Zheng, Q. Wang, F. Sun, X. Jiang, A. Pan, L. Zhang, *ACS Nano* **2017**, *11*, 10681.
[5] a) F. Fan, S. Turkdogan, Z. Liu, D. Shelhammer, C. Z. Ning, *Nat. Nanotechnol.* **2015**, *10*, 796; b) C. Zhang, C.-L. Zou, H. Dong, Y. Yan, J. Yao, Y. S. Zhao, *Sci. Adv.* **2017**, *3*, e1700225.
[6] a) W. Zhang, L. Peng, J. Liu, A. Tang, J.-S. Hu, J. Yao, Y. S. Zhao, *Adv. Mater.* **2016**, *28*, 4040; b) R.-M. Ma, R. F. Oulton, V. J. Sorger, G. Bartal, X. Zhang, *Nat. Mater.* **2011**, *10*, 110.
[7] J. Li, Y. Lin, J. Lu, C. Xu, Y. Wang, Z. Shi, J. Dai, *ACS Nano* **2015**, *9*, 6794.
[8] a) L. Chen, E. Towe, *Appl. Phys. Lett.* **2006**, *89*, 053125; b) M. P. Nesnidal, L. J. Mawst, A. Bhattacharya, D. Botez, L. DiMarco, J. C. Connolly, J. H. Abeles, *IEEE Photonics Technol. Lett.* **1996**, *8*, 182.
[9] a) J. Zhao, Y. Yan, C. Wei, W. Zhang, Z. Gao, Y. S. Zhao, *Nano Lett.* **2018**, *18*, 1241; b) H. Gao, A. Fu, S. C. Andrews, P. Yang, *Proc. Natl. Acad. Sci.* **2013**, *110*, 865; c) Y. Y. Wang, C. X. Xu, M. M. Jiang, J. T. Li, J. Dai, J. F. Lu, P. L. Li, *Nanoscale* **2016**, *8*, 16631.
[10] a) S. F. Liew, B. Redding, L. Ge, G. S. Solomon, H. Cao, *Appl. Phys. Lett.* **2014**, *104*, 231108; b) F. Gu, F. Xie, X. Lin, S. Linghu, W. Fang, H. Zeng, L. Tong, S. Zhuang, *Light: Sci. Appl.* **2017**, *6*, e17061.
[11] a) A. Guarino, G. Poberaj, D. Rezzonico, R. Degl'Innocenti, P. Guenter, *Nat. Photonics* **2007**, *1*, 407; b) M. Humar, M. Ravnik, S. Pajk, I. Muševič, *Nat. Photonics* **2009**, *3*, 595; c) L. Bi, J. Hu, P. Jiang, D. H. Kim, G. F. Dionne, L. C. Kimerling, C. A. Ross, *Nat. Photonics* **2011**, *5*, 758.
[12] W. Sun, K. Wang, Z. Gu, S. Xiao, Q. Song, *Nanoscale* **2016**, *8*, 8717.
[13] a) X. Fu, Z.-M. Liao, R. Liu, F. Lin, J. Xu, R. Zhu, W. Zhong, Y. Liu, W. Guo, D. Yu, *ACS Nano* **2015**, *9*, 11960; b) X. Han, L. Kou, X. Lang, J. Xia, N. Wang, R. Qin, J. Lu, J. Xu, Z. Liao, X. Zhang, X. Shan, X. Song, J. Gao, W. Guo, D. Yu, *Adv. Mater.* **2009**, *21*, 4937; c) C. Wang, R. Bao, K. Zhao, T. Zhang, L. Dong, C. Pan, *Nano Energy* **2015**, *14*, 364; d) G. Hu, W. Guo, R. Yu, X. Yang, R. Zhou, C. Pan, Z. L. Wang, *Nano Energy* **2016**, *23*, 27; e) X. Wen, W. Wu, C. Pan, Y. Hu, Q. Yang, Z. L. Wang, *Nano Energy* **2015**, *14*, 276.
[14] D. W. Langer, *J. Appl. Phys.* **1966**, *37*, 3530.
[15] a) Y. Xu, Q. Chen, C. Zhang, R. Wang, H. Wu, X. Zhang, G. Xing, W. W. Yu, X. Wang, Y. Zhang, M. Xiao, *J. Am. Chem. Soc.* **2016**, *138*, 3761; b) M. Saliba, S. M. Wood, J. B. Patel, P. K. Nayak, J. Huang, J. A. Alexander-Webber, B. Wenger, S. D. Stranks, M. T. Hoerantner, J. T.-W. Wang, R. J. Nicholas, L. M. Herz, M. B. Johnston, S. M. Morris, H. J. Snaith, M. K. Riede, *Adv. Mater.* **2016**, *28*, 923; c) S. A. Veldhuis, P. P. Boix, N. Yantara, M. Li, T. C. Sum, N. Mathews, S. G. Mhaisalkar, *Adv. Mater.* **2016**, *28*, 6804; d) A. Fu,

 © 2019 WILEY-VCH Verlag GmbH & Co. KGaA, Weinheim

P. Yang, *Nat. Mater.* **2015**, *14*, 557; e) A. L. Rogach, *Sci. Bull.* **2017**, *62*, 314; f) P. Fu, Q. Shan, Y. Shang, J. Song, H. Zeng, Z. Ning, J. Gong, *Sci. Bull.* **2017**, *62*, 369; g) M. Y. Gao, *Sci. Bull.* **2018**, *63*, 1241; h) J. Q. Jiao, Y. Li, W. F. Shen, S. S. Gai, J. G. Tang, Y. Wang, L. J. Huang, J. X. Liu, W. Wang, L. A. Belfiore, *Sci. Bull.* **2018**, *63*, 216.

[16] a) R. Ding, X. Zhang, X. W. Sun, *Adv. Funct. Mater.* **2017**, *27*, 1702207; b) Y.-J. Kim, T.-V. Dang, H.-J. Choi, B.-J. Park, J.-H. Eom, H.-A. Song, D. Seol, Y. Kim, S.-H. Shin, J. Nah, S.-G. Yoon, *J. Mater. Chem. A* **2016**, *4*, 756; c) Q. Dong, J. Song, Y. Fang, Y. Shao, S. Ducharme, J. Huang, *Adv. Mater.* **2016**, *28*, 2816; d) R. Ding, H. Liu, X. Zhang, J. Xiao, R. Kishor, H. Sun, B. Zhu, G. Chen, F. Gao, X. Feng, J. Chen, X. Chen, X. Sun, Y. Zheng, *Adv. Funct. Mater.* **2016**, *26*, 7708; e) S. Huang, G. Tang, H. L. Huang, X. G. Wu, P. M. Zhou, L. Zou, L. Xie, J. M. Deng, X. Y. Wang, H. Z. Zhong, J. W. Hong, *Sci. Bull.* **2018**, *63*, 1254.

[17] T. Wang, B. Daiber, J. M. Frost, S. A. Mann, E. C. Garnett, A. Walsh, B. Ehrler, *Energy Environ. Sci.* **2017**, *10*, 509.

[18] Y. Nagaoka, K. Hills-Kimball, R. Tan, R. Li, Z. Wang, O. Chen, *Adv. Mater.* **2017**, *29*, 1606666.

[19] a) S. Ippili, V. Jella, J. Kim, S. Hong, S.-G. Yoon, *Nano Energy* **2018**, *49*, 247; b) R. Ding, X. Zhang, G. Chen, H. Wang, R. Kishor, J. Xiao, F. Gao, K. Zeng, X. Chen, X. W. Sun, Y. Zheng, *Nano Energy* **2017**, *37*, 126; c) R. Saraf, L. Pu, V. Maheshwari, *Adv. Mater.* **2018**, *30*, 1705778; d) J. Xiao, J. Chang, B. Li, F. H. Isikgor, D. Wang, Z. Fan, Z. Lin, J. Ouyang, K. Zeng, J. Chen, *J. Mater. Chem. A* **2018**, *6*, 9665; e) Q. Lai, L. Zhu, Y. Pang, L. Xu, J. Chen, Z. Ren, J. Luo, L. Wang, L. Chen, K. Han, P. Lin, D. Li, S. Lin, B. Chen, C. Pan, Z. L. Wang, *ACS Nano* **2018**, *12*, 10501.

[20] a) Y. Wang, X. Li, V. Nalla, H. Zeng, H. Sun, *Adv. Funct. Mater.* **2017**, *27*, 1605088; b) Z. Liu, J. Yang, J. Du, Z. Hu, T. Shi, Z. Zhang, Y. Liu, X. Tang, Y. Leng, R. Li, *ACS Nano* **2018**, *12*, 5923; c) X. Wang, M. Shoaib, X. Wang, X. Zhang, M. He, Z. Luo, W. Zheng, H. Li, T. Yang, X. Zhu, L. Ma, A. Pan, *ACS Nano* **2018**, *12*, 6170; d) Z. Yang, Q. Xu, X. Wang, J. Lu, H. Wang, F. Li, L. Zhang, G. Hu, C. Pan, *Adv. Mater.* **2018**, *30*, 1802110.

[21] a) S. W. Eaton, M. Lai, N. A. Gibson, A. B. Wong, L. Dou, J. Ma, L.-W. Wang, S. R. Leone, P. Yang, *Proc. Natl. Acad. Sci.* **2016**, *113*, 1993; b) D. Zhang, S. W. Eaton, Y. Yu, L. Dou, P. Yang, *J. Am. Chem. Soc.* **2015**, *137*, 9230.

[22] Y. Rakita, N. Kedem, S. Gupta, A. Sadhanala, V. Kalchenko, M. L. Bohm, M. Kulbak, R. H. Friend, D. Cahen, G. Hodes, *Cryst. Growth Des.* **2016**, *16*, 5717.

[23] Q. Liao, K. Hu, H. Zhang, X. Wang, J. Yao, H. Fu, *Adv. Mater.* **2015**, *27*, 3405.

[24] a) X. Lao, Z. Yang, Z. Su, Z. Wang, H. Ye, M. Wang, X. Yao, S. Xu, *Nanoscale* **2018**, *10*, 9949; b) W. Du, S. Zhang, Z. Wu, Q. Shang, Y. Mi, J. Chen, C. Qin, X. Qiu, Q. Zhang, X. Liu, *Nanoscale* **2019**, *11*, 3145; c) A. Dey, P. Rathod, D. Kabra, *Adv. Opt. Mater.* **2018**, *6*, 1800109.

© 2019 WILEY-VCH Verlag GmbH & Co. KGaA, Weinheim